ADVANCED MATERIALS
www.advmat.de

# Atomically Isolated Rh Sites within Highly Branched $Rh_2Sb$ Nanostructures Enhance Bifunctional Hydrogen Electrocatalysis

*Ying Zhang, Gen Li, Zhonglong Zhao, Lili Han, Yonggang Feng, Shangheng Liu, Bingyan Xu, Honggang Liao,* Gang Lu, Huolin L. Xin,* and Xiaoqing Huang**

**Breaking the bottleneck of hydrogen oxidation/evolution reactions (HOR/HER) in alkaline media is of tremendous importance for the development of anion exchange membrane fuel cells/water electrolyzers. Atomically dispersed active sites are known to exhibit excellent activity and selectivity toward diverse catalytic reactions. Here, a class of unique $Rh_2Sb$ nanocrystals with multiple nanobranches (denoted as $Rh_2Sb$ NBs) and atomically dispersed Rh sites are reported as promising electrocatalysts for alkaline HOR/HER. $Rh_2Sb$ NBs/C exhibits superior HER performance with a low overpotential and a small Tafel slope, outperforming both Rh NBs/C and commercial Pt/C. Significantly, $Rh_2Sb$ NBs show outstanding HOR performance of which the HOR specific activity and mass activity are about 9.9 and 10.1 times to those of Rh NBs/C, and about 4.2 and 3.7 times to those of Pt/C, respectively. Strikingly, $Rh_2Sb$ NBs can also exhibit excellent CO tolerance during HOR, whose activity can be largely maintained even at 100 ppm CO impurity. Density functional theory calculations reveal that the unsaturated Rh sites on $Rh_2Sb$ NBs surface are crucial for the enhanced alkaline HER and HOR activities. This work provides a unique catalyst design for efficient hydrogen electrocatalysis, which is critical for the development of alkaline fuel cells and beyond.**

## 1. Introduction

Hydrogen, as a clean and renewable energy resource, has been deemed as a promising alternative to the traditional fossilfuels in electrochemical energy storage and conversion system.[1–3] To realize the efficient reversible hydrogen generation and utilization for a successful hydrogen economy, hydrogen electrode reactions, involving hydrogen evolution reaction (HER) in water electrolysis and hydrogen oxidation reaction (HOR) in fuel cells, have been intensively investigated.[4–10] With the rapid development of anion exchange membrane for alkaline fuel cells, HOR/HER in alkaline media has attracted increasing attention due to their more benign reaction conditions compared to proton exchange membrane fuel cells.[11–16] However, the HOR/HER activities of Pt-group catalysts in alkaline media have been demonstrated two orders of magnitude lower than those in acidic media, which becomes one of the major barriers for the breakthrough of anion exchange membrane fuel cells.[17,18] Therefore, it is imperative to develop robust HER/HOR catalysts to drive those two reactions in alkaline media to satisfy the practically relevant rates.

From the volcano diagram of calculated hydrogen adsorption energies and experimentally measured exchange currents based on different transition and noble metals, Rh has been considered as one of the most promising alternatives to Pt in the HOR/HER reaction.[19] However, the performance of many reported Rh-based catalysts for HOR/HER is still not sufficient to meet practical applications.[20–22] Recently, it has been reported that catalysts with atomically isolated sites generally exhibit excellent activity and selectivity for various catalytic reactions due to their optimal adsorption with reactants and products.[23–26] However, the conventional single-atom catalysts are particularly vulnerable under the harsh electrocatalytic reaction conditions.[27] To enhance the stability of single atom catalysts, one popular strategy is to isolate the single site with another metal, on which the single sites can be anchored and stabilized by other metal atoms.[28] Therefore, it is extremely desirable to create Rh-based alloy catalysts, which could simultaneously possess atomically

Y. Zhang, G. Li, Y. Feng, S. Liu, B. Xu, H. Liao, X. Huang
State Key Laboratory of Physical Chemistry of Solid Surfaces
College of Chemistry and Chemical Engineering
Xiamen University
Xiamen 361005, China
E-mail: hgliao@xmu.edu.cn; hxq006@xmu.edu.cn
Z. Zhao
School of Physical Science and Technology
Inner Mongolia University
Hohhot 010021, China
L. Han, H. L. Xin
Department of Physics and Astronomy
University of California
Irvine, CA 92697, USA
E-mail: huolinx@uci.edu
G. Lu
Department of Physics and Astronomy
California State University
Northridge, CA 91330, USA
The ORCID identification number(s) for the author(s) of this article can be found under https://doi.org/10.1002/adma.202105049.

**DOI: 10.1002/adma.202105049**

 

isolated surface sites for activity enhancement and robust structure for high stability, but there is rare report on this respect.

Herein, we explored a class of highly branched $Rh_2Sb$ nanocrystals (denoted as $Rh_2Sb$ NBs) with atomically isolated Rh sites for efficient alkaline hydrogen electrocatalysis. The detailed characterizations demonstrated that $Rh_2Sb$ NBs with high yield were composed of many {210} facets of $Rh_2Sb$ phase. Benefited from their unique structure, $Rh_2Sb$ NBs/C could serve as highly efficient catalysts for both alkaline HOR and HER. $Rh_2Sb$ NBs/C exhibits excellent alkaline HER performance with a low overpotential of 39.5 mV at 10 mA $cm^{-2}$ and a small Tafel slope of 40.1 mV $dec^{-1}$, outperforming both Rh NBs/C and commercial Pt/C. In particular, the HOR mass activity ($J_{k,m}$) and specific activity ($J_{k,s}$) is ≈10.1 and ≈9.9 times to those of Rh NBs/C, and ≈3.7 and ≈4.2 times to those of Pt/C, respectively. More significantly, $Rh_2Sb$ NBs/C can also display excellent CO tolerance in alkaline HOR. By combining electrochemical tests and theoretical calculations, we concluded that the unsaturated surface sites on $Rh_2Sb$ NBs played a vital role in enhancing alkaline HER and HOR activities.

## 2. Results and Discussion

The $Rh_2Sb$ NBs were synthesized through a hydrothermal process with rhodium (III) 2,4-pentanedionate ($Rh(acac)_3$) and antimony trichloride ($SbCl_3$) as metal precursors, polyvinyl pyrrolidone as surfactant, and benzyl alcohol (BP) as solvent in the presence of ammonia bromide ($NH_4Br$) (see Supporting Information for details). High-angle annular dark-field scanning transmission electron microscopy (HAADF-STEM) image shows that uniform $Rh_2Sb$ NBs with high morphological yield were obtained (**Figure 1**A and Figure S1, Supporting Information). High-magnification TEM image vividly depicted the branched

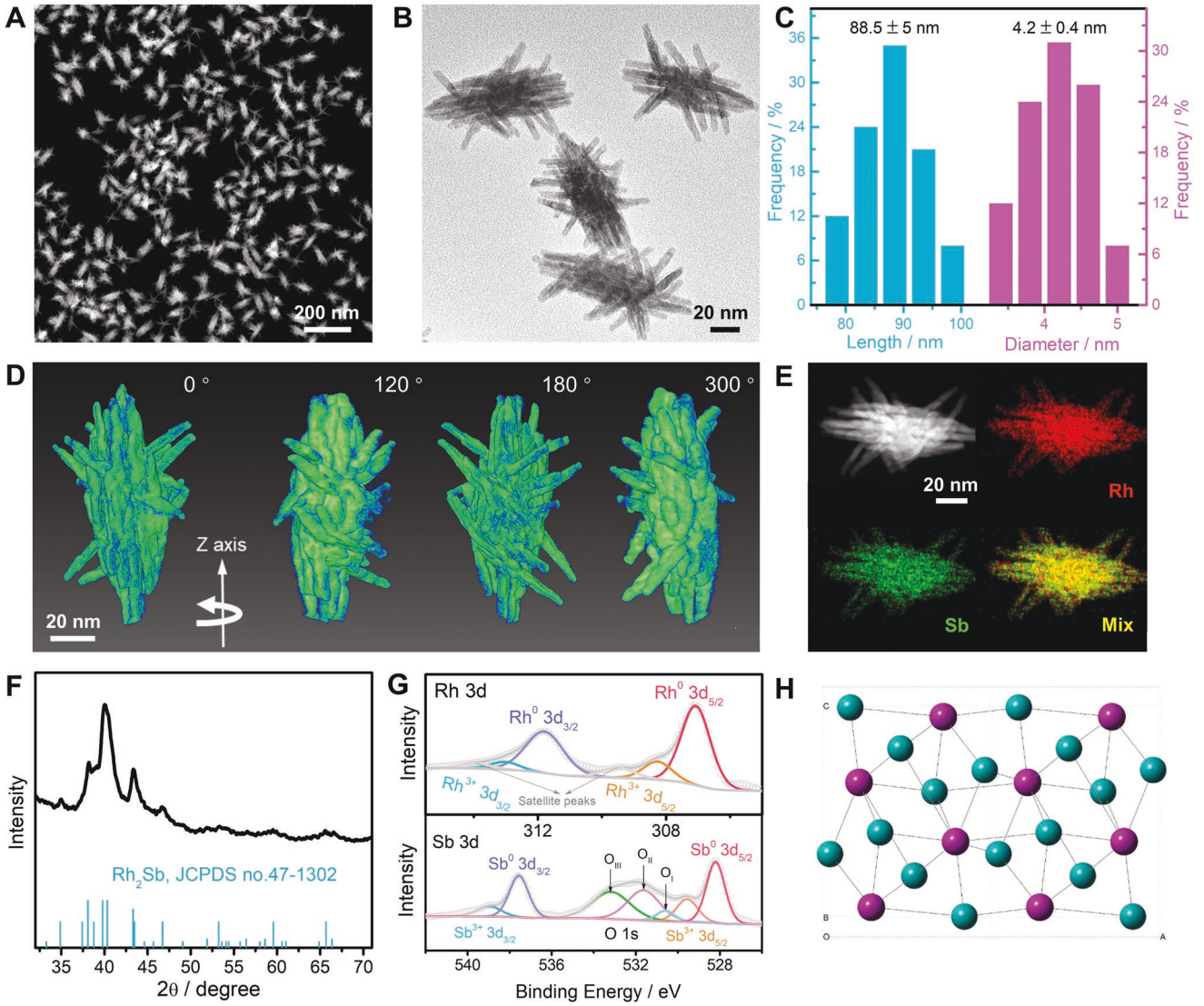


**Figure 1.** A) HAADF-STEM image and B) TEM image, C) length and diameter distribution, D) three projected 3D visualizations of tomographic reconstruction images at viewing angles of 0°, 120°, 180°, and 300°. E) Elemental mappings of $Rh_2Sb$ NBs: HAADF-STEM image, Rh mapping in red, Sb mapping in green, and integrated mapping of Rh and Sb are shown. F) PXRD pattern and G) XPS spectra of Rh 3d, Sb 3d, and O 1s of $Rh_2Sb$ NBs. H) Crystal structure of $Rh_2Sb$ along [010] plane, dark cyan and purple spheres denote Rh and Sb atoms, respectively.

features of $Rh_2Sb$ NBs (Figure 1B), and the mean length and diameter of those branches were ≈88.5 and ≈4.2 nm, respectively (Figure 1C). To reveal the growth mechanism of the $Rh_2Sb$ NBs, the $Rh_2Sb$ NBs intermediates were collected at different reaction times. Figure S2, Supporting Information, shows TEM images of the intermediates. At the initial stage (<15 min), the products with branch shape are already observed and the size gradually increases (Figure S2A–D, Supporting Information). The branch shape of products become more obvious with the reaction time increase to 30 min (Figure S2E, Supporting Information). After 60 min, uniform $Rh_2Sb$ NBs are obtained (Figure S2F, Supporting Information). Further extension of the reaction time to 120 min or even 180 min does not result in obvious morphological changes (Figure S2G,H, Supporting Information). The above results demonstrate the $Rh_2Sb$ NBs is not simply assembled by nanorods but an integrated body.

To further identify the overall morphology of NBs, we applied 3D tomographic reconstruction of $Rh_2Sb$ NBs from different angles. We can see that the $Rh_2Sb$ NBs were assembled by multiple nanobranches splay out wildly in different directions (Figure 1D). Elemental mapping images suggested that Rh and Sb were evenly distributed in $Rh_2Sb$ NBs (Figure 1E). The peaks in X-ray diffraction pattern were ascribed to $Rh_2Sb$ alloy (JCPDS: 47–1302) (Figure 1F).[29] Moreover, scanning electron microscopy energy-dispersive X-ray spectroscopy (SEM-EDS) showed that the atomic ratio of Rh to Sb was close to 2, which is consistent with the value obtained from inductively coupled plasma optical emission spectrometer measurement (66.1/33.9) (Figure S3, Supporting Information). X-ray photoelectron spectroscopy (XPS) measurement was performed to reveal the surface properties of $Rh_2Sb$ NBs (Figure 1G). It was found that Rh and Sb were mainly in metal state with partial oxidation on surface ($Rh^{3+}$ and $Sb^{3+}$). The O 1s peak in Sb 3d XPS spectrum can fit with three characteristic $O_I$, $O_{II}$, and $O_{III}$ peaks at 530.5, 531.6, and 533.2 eV, corresponding to the lattice oxygen in metal oxide, defect-oxide/hydroxyl-like groups, and unavoidable surface physically adsorbed/residual water molecules, respectively. We further calculated the atomic ratios of $Rh^{3+}/Rh^0$ and $Sb^{3+}/Sb^0$ based on the peak fittings of XPS spectra (Table S1, Supporting Information). It was noted that the binding energy of Rh $3d_{5/2}$ peak negatively shifted by ≈0.29 eV compared to Rh NBs (Figure S4, Supporting Information),[30] indicating that electrons might transfer from Sb to Rh. Considering Rh atoms were isolated by Sb atoms in the crystalline structure of $Rh_2Sb$ alloy (Figure 1H), we concluded that Rh atoms presented as single states.[28,31]

To elucidate the detailed structural information for $Rh_2Sb$ NBs, X-ray absorption fine structure (XAFS) spectroscopy analysis and aberration-corrected HAADF-STEM measurement were further performed. X-ray absorption near-edge structure analysis shows that the Rh absorption energy for $Rh_2Sb$ NBs is close to Rh powder (**Figure 2**A), indicating the existence of metallic state of Rh in $Rh_2Sb$ NBs, in agreement with the XPS results. The Fourier-transformed $k^3\chi(k)$ functions of extended XAFS spectra in frequency domain (R) space reveal the information on coordination environment. The $Rh_2Sb$ NBs show the main peak at ≈2.33 Å, which corresponds to the Rh—Sb bond (Figure 2B). As for Rh powder and $Rh_2O_3$ powder, a main peak of Rh—Rh and Rh—O coordination were observed at 2.58 and 1.60 Å, respectively. No Rh—Rh characteristic peaks can be detected for $Rh_2Sb$ NBs, confirming the isolated Rh sites within the branched $Rh_2Sb$ nanostructures. Figure 2C–E shows the atomically resolved HAADF-STEM images, oriented along $[0\bar{2}1]$, $[10\bar{1}]$, and [001] zone axes. Corresponding fast Fourier transform patterns (Figure $2C_1$–$E_1$) agree with the standard structure mode (ICSD no. 42960), indicating that $Rh_2Sb$ NBs possesses orthorhombic crystal structure (space group: Pnma, no. 62). Figure $2C_2$–E2 exhibits ideal crystal structure models of $Rh_2Sb$, along three corresponding zone axes. The atomic structure modes (inset in Figure 2C–E) match well with HAADF-STEM images. We then performed aberration-corrected high-resolution TEM (AC-HRTEM) to carefully identify the surface structure of $Rh_2Sb$ NBs. AC-HRTEM images (Figure 2F,G) suggest that $Rh_2Sb$ NBs are single crystal and grow along <001> direction. The exposed surfaces are mainly {210} high-index facets.[32] As revealed by the atomic structure modes (inset in Figure 2F,G), Rh atoms of the {210} facet are isolated by Sb atoms. The d-band center of $Rh_2Sb$ NBs is analyzed by the XPS spectra (Figure S5, Supporting Information). We find that there is an upshift of the d-band center of the surface Rh atoms on $Rh_2Sb$ NBs, which essentially derived from the charge transfers between Rh and Sb (as shown in Table S1, Supporting Information). The upshift of the d-band center will increase the adsorption of $H_2O$ and lower the barrier for $H_2O$ dissociation.

To investigate the unique $Rh_2Sb$ structure on catalytic performance, we chose electrochemical HER and HOR as model reactions. Prior to catalytic test, $Rh_2Sb$ NBs were loaded on commercial carbon black (C, Vulcan XC-72R) ($Rh_2Sb$ NBs/C, Figure S6, Supporting Information) and benchmarked with Rh NBs/C (Figure S7, Supporting Information) and commercial Pt/C (JM, 20 wt% Pt). The catalysts were dispersed in a mixture of isopropanol/Nafion, and then dropped onto glassy carbon electrode (area: 0.196 $cm^2$). The loading amount of Rh (or Pt) was kept to be 10.0 μg $cm^{-2}$ for all catalysts. Cyclic voltammograms (CVs) were conducted in Ar-saturated 0.1 M KOH at a scan rate of 50 mV $s^{-1}$. It was found that the hydrogen desorption potential of $Rh_2Sb$ NBs/C and Rh NBs/C was 0.37 V, which was lower than that of Pt/C (0.47 V) (Figure S8, Supporting Information), indicating that the adsorption of hydrogen species on $Rh_2Sb$ NBs/C and Rh NBs/C was weaker than that on Pt/C, and as a major reason of enhancements in HER/HOR activities.[33] CO-stripping measurements revealed that the electrochemically active surface areas (ECSAs) of $Rh_2Sb$ NBs/C in 0.1 M KOH, Rh NBs/C and Pt/C were 58.0, 56.5, and 67.3 $m^2$ $g^{-1}$, close to calculated value in 0.1 M $HClO_4$ (Figure S9A,C, Supporting Information). Additionally, compared to the positions of CO-oxidation peak for Rh NBs/C (0.67 V) and Pt/C (0.65 V), the position of CO oxidation peak for $Rh_2Sb$ NBs/C shifted to low potential (0.61 V) (Figure S9B, Supporting Information). However, the CO oxidation peak potential of the $Rh_2Sb$ NBs/C (0.69 V) is lower in acidic medium than Rh NBs/C (0.72 V) and Pt/C (0.87 V) (Figure S9D, Supporting Information), suggesting that $Rh_2Sb$ NBs/C possessed superior resistance to CO poisoning in both acidic and alkaline media. It is believed that Sb can form oxidation species at low potential, which can promote the oxidation of CO adsorbed on adjacent Rh sites.[34]

We initially applied $Rh_2Sb$ NBs/C to HER catalysis under alkaline media. **Figure 3**A shows the HER polarization curves

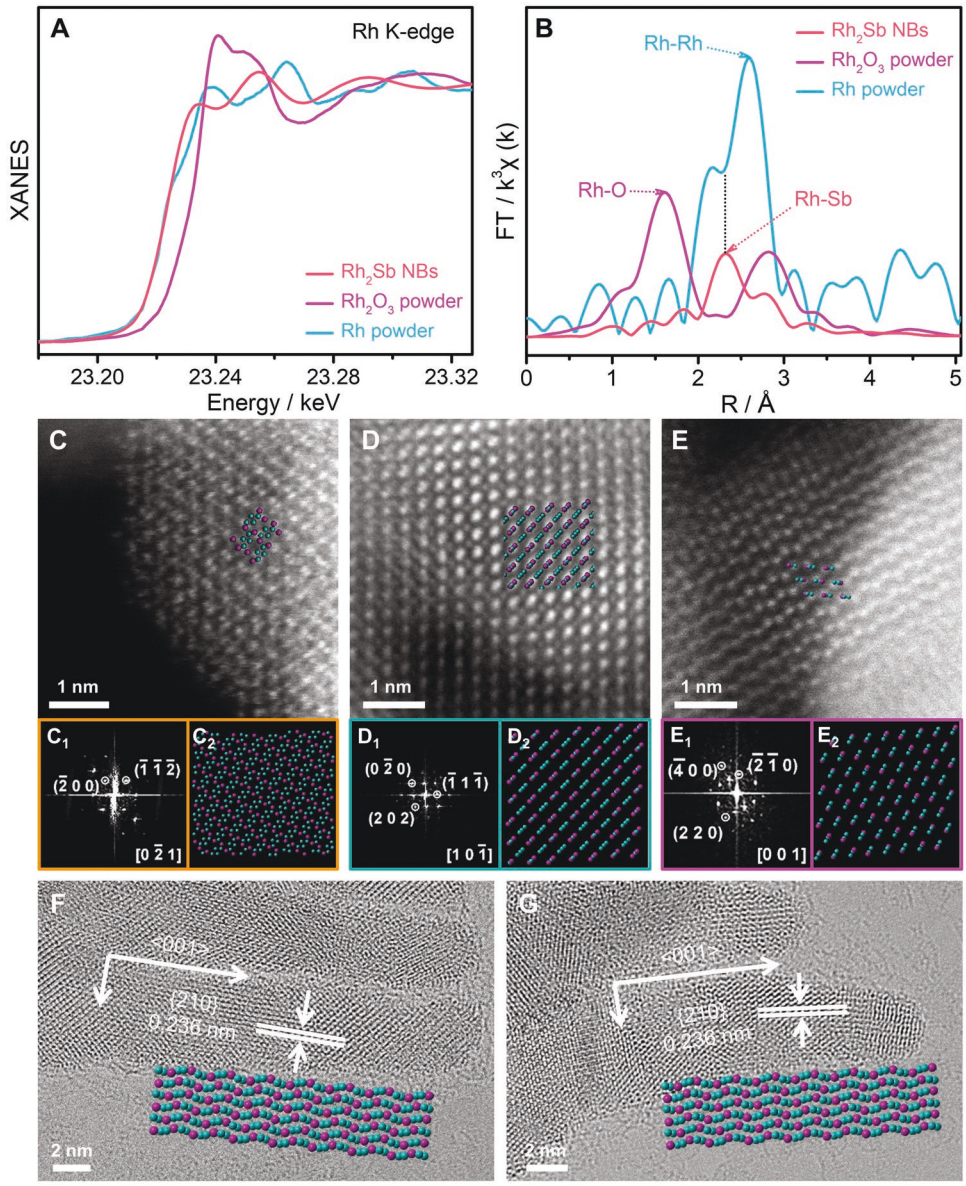


**Figure 2.** Normalized Rh K-edge A) XANES and B) EXAFS spectra of Rh powder, $Rh_2O_3$ powder, and $Rh_2Sb$ NBs. C–E) HAADF-STEM images oriented along [0$\bar{2}$1], [10$\bar{1}$], and [001] zone axes. The insert (C–E) shows HAADF-STEM images match well with atomic modes. $C_1$–$E_1$) Corresponding FFT patterns and $C_2$–$E_2$) ideal crystal modes. F,G) HRTEM images and atomic modes of {210} facets.

of $Rh_2Sb$ NBs/C, Rh NBs/C, and commercial Pt/C in 0.1 M KOH with a scan rate of 5 mV $s^{-1}$. Primarily, the number of active site and turnover frequencies (TOF) value were calculated to reveal the intrinsic activity based on the CO stripping in 0.1 M KOH (Table S2, Supporting Information). As observed in Figure 3A, the TOF value of $Rh_2Sb$ NBs/C at the overpotential of 50 mV was 6.36 $H_2$ $s^{-1}$, higher than those of Rh NBs/C (0.77 $H_2$ $s^{-1}$ at 50 mV) and Pt/C (1.76 $H_2$ $s^{-1}$ at 50 mV). The overpotentials of $Rh_2Sb$ NBs/C, Rh NBs/C, and commercial Pt/C were 39.5, 134.0, and 79.4 mV, respectively, at a current density of 10 mA $cm^{-2}$. The Tafel slope of $Rh_2Sb$ NBs/C was 40.1 mV $dec^{-1}$, which was much lower than those of Rh NBs/C (132.2 mV $dec^{-1}$) and Pt/C (58.9 mV $dec^{-1}$), implying the fastest HER kinetics compared to Rh NBs/C and Pt/C (Figure 3B). Furthermore, we also compared the current density of each catalyst under different overpotentials (Figure 3C). It was found that the current density of $Rh_2Sb$ NBs/C was 21.9 mA $cm^{-2}$) at 60 mV, which was ≈9.5 and ≈3.2 times to those of Rh NBs/C (2.3 mA $cm^{-2}$) and Pt/C (6.9 mA $cm^{-2}$), respectively. To the best of our knowledge, the HER performance of $Rh_2Sb$ NBs/C has outperformed many other reported catalysts (Table S3, Supporting Information). Furthermore, the stability of $Rh_2Sb$ NBs/C for HER was evaluated by 1000-cycle accelerated durability tests in 0.1 M KOH. The overpotential was slightly increased by 2.3 mV at 10 mA $cm^{-2}$, suggesting the promising stability of $Rh_2Sb$ NBs/C for HER (Figure 3D and Figure S10, Supporting Information). In addition, the HER performance of various catalysts was also investigated under acidic conditions. It was found that

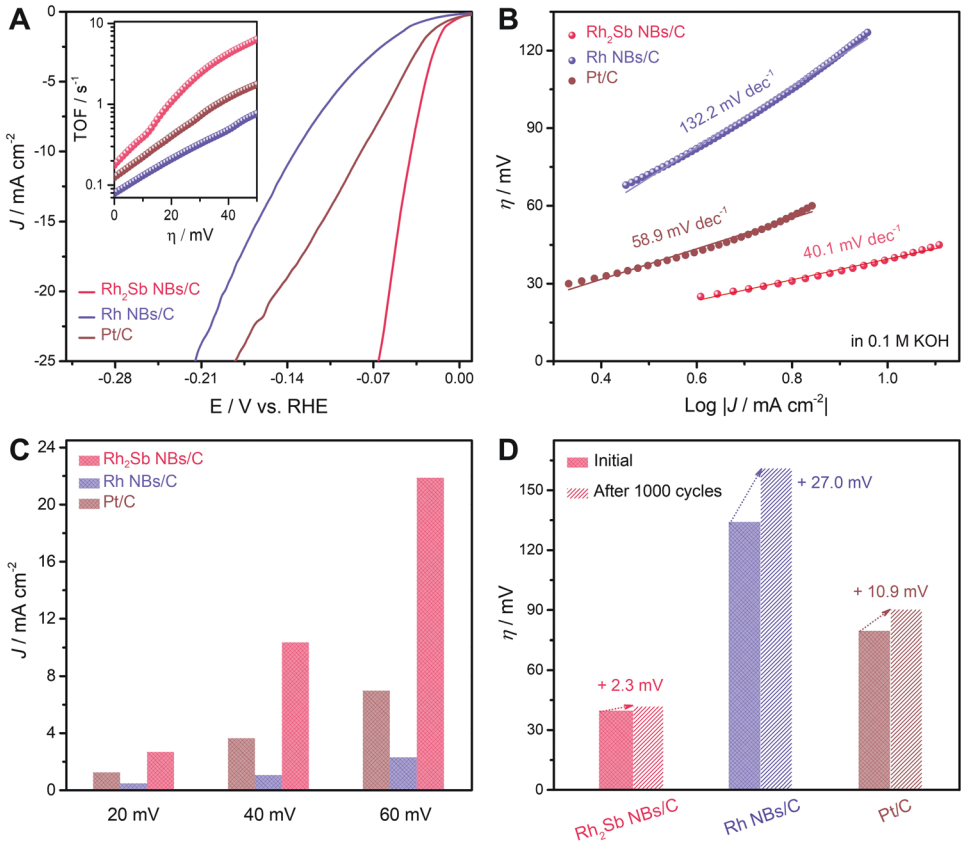


**Figure 3.** A) HER polarization curves and B) Tafel plots of $Rh_2Sb$ NBs/C, Rh NBs/C, and Pt/C in Ar-saturated 0.1 M KOH with a scan rate of 5 mV $s^{-1}$, inset (A) is TOF values of HER of different catalysts. C) The current density of HER at different overpotentials. D) Histograms of comparative overpotentials for the $Rh_2Sb$ NBs/C, Rh NBs/C, and Pt/C before and after 1000 cycles of ADTs.

$Rh_2Sb$ NBs/C displayed lower overpotential (28.3 mV) and Tafel slope (24.6 mV $dec^{-1}$) than Rh NBs/C and Pt/C (Figure S11, Supporting Information), suggesting that $Rh_2Sb$ NBs/C could also sever as an efficient catalyst for acidic HER.

Encouraged by the enhanced performance of the $Rh_2Sb$ NBs/C for alkaline HER, we further explored its electrocatalytic performance toward the anodic HOR. **Figure 4**A shows the HOR polarization curves of various catalysts normalized by the area of glassy carbon area (0.196 $cm^2$), which were conducted in $H_2$-saturated 0.1 M KOH solution at a sweep rate of 5 mV $s^{-1}$ and at a rotation rate of 1600 rpm with rotating disk electrode (RDE). As showed in Figure 4A and Figure S12, Supporting Information, $Rh_2Sb$ NBs/C exhibited much faster kinetics and intrinsic activity than Rh NBs/C and commercial Pt/C for HOR. Figure 4B shows the ECSA normalized kinetic current density (*J*k) versus the potential via the Butler-Volmer fittings. $Rh_2Sb$ NBs/C displayed high kinetic current densities under different overpotentials, suggesting the promising HOR activity of $Rh_2Sb$ NBs/C for HOR. Meanwhile, Butler-Volmer equation was used to obtain the exchange current density (*J*0) for investigating the intrinsic activity. As shown in Figure 4C,D and Figure S13, Supporting Information, the Koutecky–Levich plots at 0.10 V showed that the inverse of current density was linear with the inverse of square root of the rotating rate, and the slope of Koutecky–Levich plot for $Rh_2Sb$ NBs/C was calculated to be 12.64 $cm^2$ $mA^{-1}$ $rpm^{1/2}$, and the electron-transfer number was approximatively calculated to be 2.0, indicating that HOR on $Rh_2Sb$ NBs/C was nearly two-electron process.[35] *J*0 and *J*k were further normalized by the metal mass and ECSA, which were denoted as *J*0,m, *J*k,m, and *J*0,s, *J*k,s, respectively. As shown in Figure 4E, *J*0,s and *J*0,m of $Rh_2Sb$ NBs/C were calculated to be 0.506 and 0.462 mA $\mu g_{PGM}^{-1}$, respectively, which were much higher than those of Rh NBs/C (0.146 and 0.130 mA $\mu g_{PGM}^{-1}$) and Pt/C (0.250 and 0.264 mA $\mu g_{PGM}^{-1}$). In addition, *J*k,s and *J*k,m of $Rh_2Sb$ NBs/C at 50 mV were 3.568 and 3.254 mA $\mu g_{PGM}^{-1}$, respectively (Figure 4F), which were about 9.9 and 10.1 times to those of Rh NBs/C (0.361 and 0.321 mA $\mu g_{PGM}^{-1}$), and about 4.2 and 3.7 times to those of Pt/C (0.840 and 0.887 mA $\mu g_{PGM}^{-1}$), respectively (Table S4, Supporting Information). We have compared the HOR performance of the Rh NBs/C with the recent reported electrocatalysts (Table S5, Supporting Information). It is clear to see that the $Rh_2Sb$ NBs exhibit the impressive performance toward alkaline HOR.

We further evaluated the durability of $Rh_2Sb$ NBs/C, Rh NBs/C, and commercial Pt/C by applying chronoamperometry at 0.10 V versus RHE operated on catalyst-modified RDE. After a continuous 20 000 s operation in $H_2$-saturated 0.1 M KOH, $Rh_2Sb$ NBs/C exhibited a decay of current density by ≈6.5%, which was much small than that of Rh NBs/C (71.2%) and Pt/C (49.2%) (**Figure 5**A). Moreover, the spent $Rh_2Sb$ NBs/C was characterized by TEM and SEM-EDS measurements (Figure S14, Supporting Information). The morphology and composition

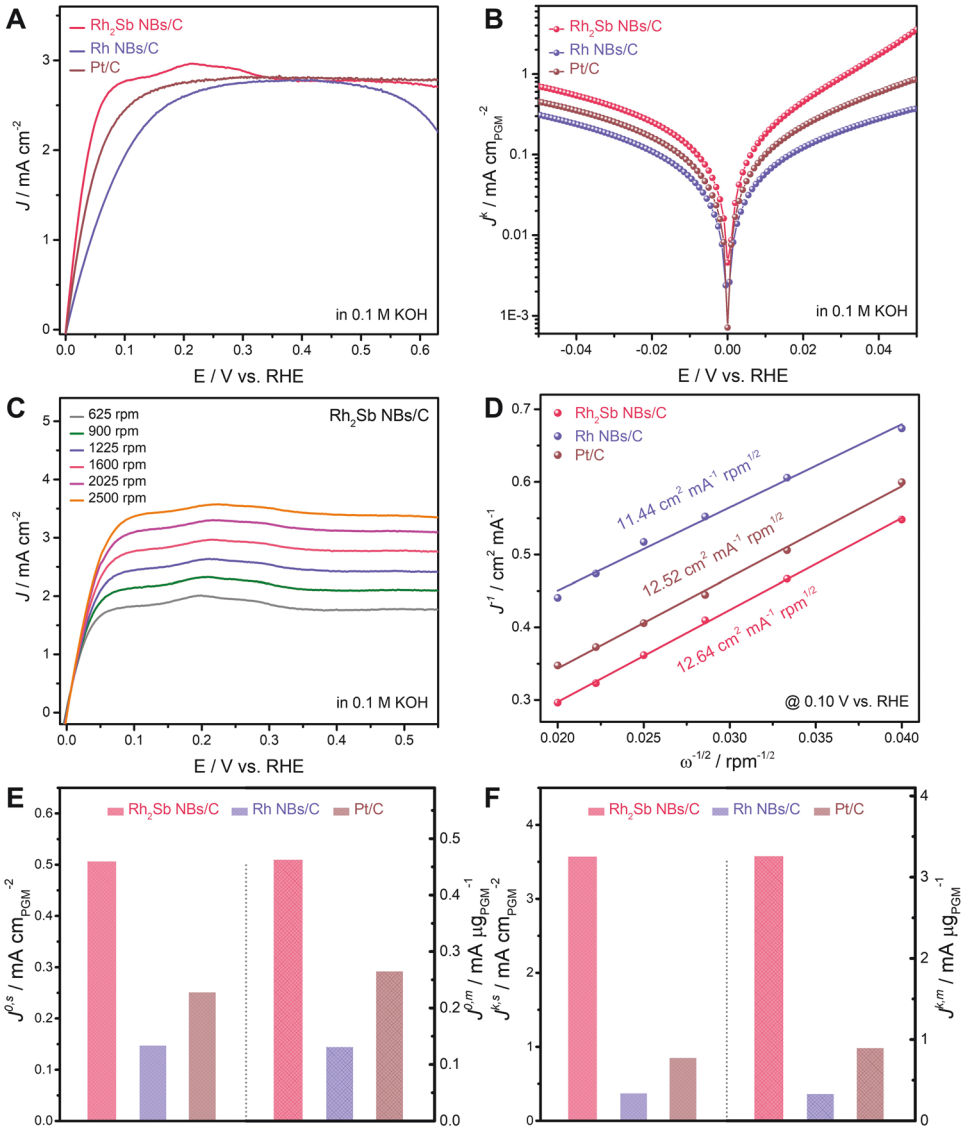


**Figure 4.** A) HOR polarization curves of $Rh_2Sb$ NBs/C, Rh NBs/C, and Pt/C in $H_2$-saturated 0.1 M KOH with a scan rate of 5 mV $s^{-1}$ at the rotating speed of 1600 rpm. B) The Tafel plots of the ECSA normalized kinetic current densities (*J*k) via the Butler-Volmer fittings. C) HOR polarization curves of $Rh_2Sb$ NBs/C at the rotating speeds varied from 2500 to 625 rpm. D) Koutecky–Levich plots at overpotentials of 0.10 V versus RHE. E) Exchange current densities and F) kinetic current densities (at 50 mV) normalized by ECSA or metal mass.

of the spent $Rh_2Sb$ NBs/C were largely maintained, whereas severe aggregations occurred for the spent Rh NBs/C and commercial Pt/C (Figure S15, Supporting Information). Considering the existence of trace amount of CO in the actual low-temperature hydrogen-oxygen fuel cell,[36] the resistance to CO poisoning of catalyst was therefore further investigated.[37] Compared to the obvious decays in the current densities for Rh NBs/C and Pt/C in the presence of 100 ppm CO, $Rh_2Sb$ NBs/C displayed a much smaller decay in current density from HOR polarization curves (Figure S16, Supporting Information). Moreover, the durability of catalysts was evaluated using chronoamperometry at 0.10 V versus RHE in $H_2$-saturated 0.1 M KOH with 100 ppm CO. As shown in Figure 5B, the relative current density for HOR on $Rh_2Sb$ NBs/C decreased by 11.2% after continuous operation for 5000 s, which was much lower than that of Rh NBs/C (29.7%) and Pt/C (49.1%) under the same conditions. Further increasing CO to 1000 ppm led complete deactivations of commercial Pt/C after 1500 s, while the HOR activity of $Rh_2Sb$ NBs/C dropped by 45.5% at 2000 s (Figure S17, Supporting Information), suggesting the superior stability against CO poisoning of $Rh_2Sb$ NBs/C to commercial Pt/C.

To elucidate the origin of enhanced alkaline HER and HOR activities on the $Rh_2Sb$ NBs, density functional theory (DFT) calculations were carried out. It is established that the overall HER/HOR reaction involves three elementary steps, that is, the Tafel or Heyrovsky reaction for $H_2$ formation (dissociation) and the Volmer step for $H_2O$ dissociation (formation).[38] Despite the lack of complete understandings on the effects of electrolyte pH values on HOR/HER activities, recent studies suggested

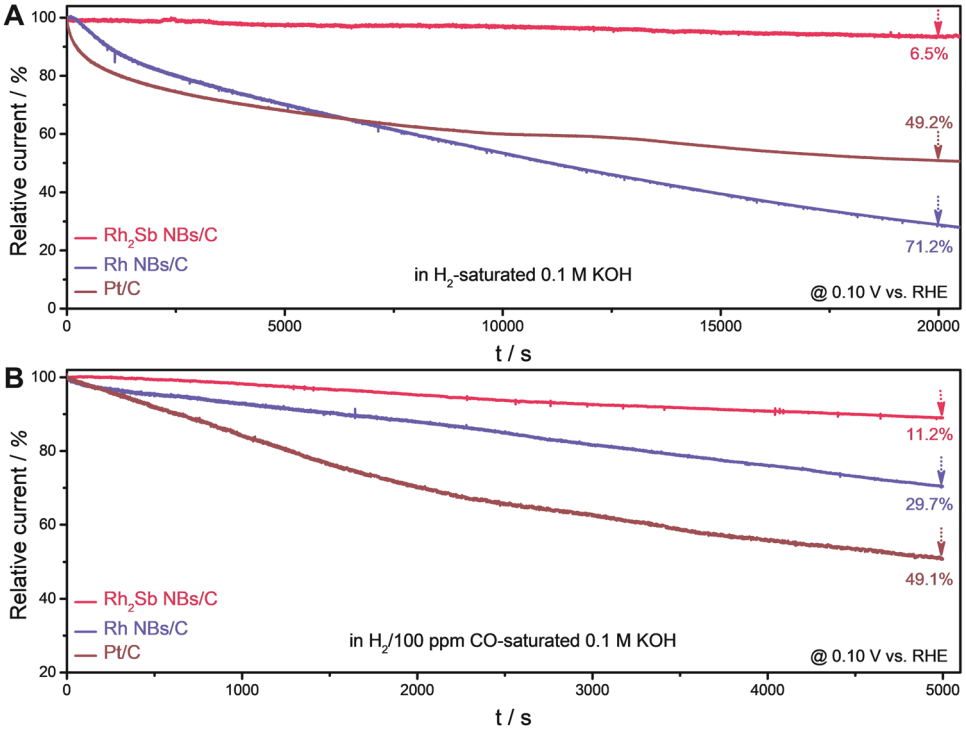


**Figure 5.** Relative current-time chronoamperometry response of $Rh_2Sb$ NBs/C, Rh NBs/C, and Pt/C in A) $H_2$-saturated and B) $H_2$/100 ppm CO-saturated 0.1 M KOH solution at 0.10 V versus RHE operated on an RDE.

that the Volmer reaction was the rate-determining step for HER/HOR in alkaline electrolytes due to its higher energy barrier in splitting (formation) of $H_2O$.[39,40] Therefore, we aim to determine the dissociation energy barrier of $H_2O$ into adsorbed H and OH on $Rh_2Sb$ (210) surface and compare it with that on Pt (111) surface. $Rh_2Sb$ (210) surface comprises zigzag Rh-Sb steps, with unsaturated Rh and Sb reaction sites (**Figure 6**A). Among all available $H_2O$ adsorption sites, these unsaturated

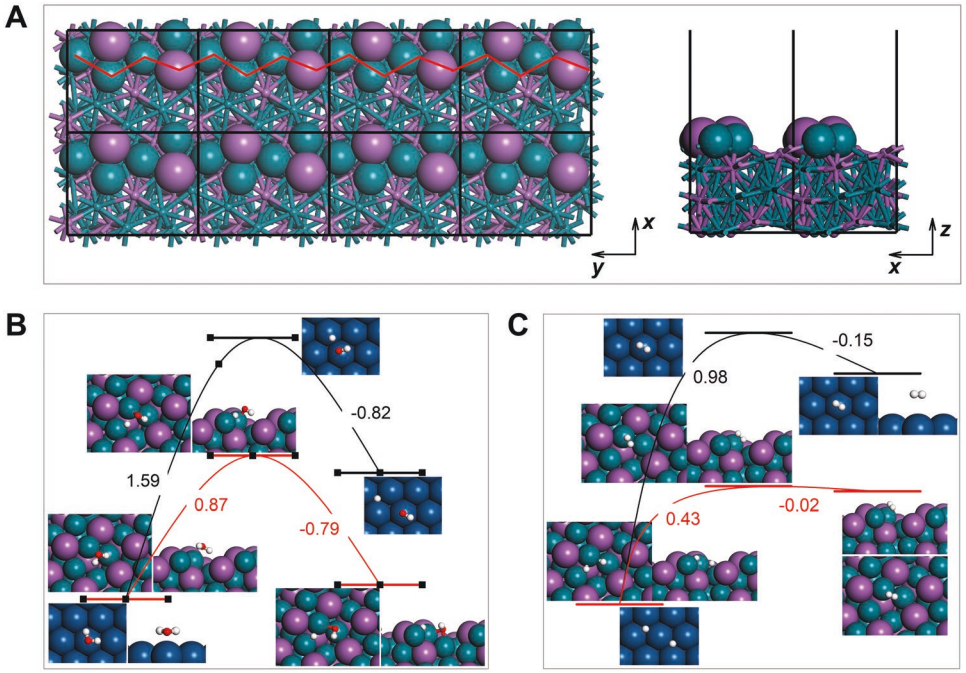


**Figure 6.** A) Atomistic slab models for $Rh_2Sb$ (210) surface. B) The energy barrier for breaking OH—H bond in the Volmer step (water dissociation) on Pt (111) and $Rh_2Sb$ (210) surfaces. C) The energy barrier for combining two $H_{ad}$ into $H_2$ (the Tafel step) on Pt (111) and $Rh_2Sb$ (210) surfaces. Top and side views of the adsorption structure of initial, transition, and final states are shown as insets. Dark cyan, purple, red, and white spheres denote Rh, Sb, O, and H atoms, respectively.

Rh atoms at $Rh_2Sb$ (210) steps were found to be most stable. Moreover, they were predicted to have even stronger $H_2O$ adsorption than active sites on the flat Pt (111) surface. More specifically, the surface-O (in $H_2O$) distance on $Rh_2Sb$ (210) step was estimated as 2.28 Å, which was shorter than that on Pt (111) surface (2.44 Å). As a result, the energy barrier for breaking the H—OH bond of $H_2O$ on $Rh_2Sb$ (210) step was 0.87 eV, which was much lower than that on Pt (111) surface (1.59 eV), as shown in Figure 6B. Interestingly, the formation of $H_2$ from the adsorbed H, in the next step of Volmer-Tafel HER reaction, followed the same trend. As shown in Figure 6C, the surface-$H_2$ distance at $Rh_2Sb$ (210) step was 1.72 Å, which was much shorter than that (3.46 Å) on flat (111) Pt surface. As a result, $H_2$ adsorption on $Rh_2Sb$ (210) step is much stronger than that on flat (111) Pt surface, leading to a lower reaction energy and a much lower $H_2$ formation barrier (0.43 versus 0.98 eV) compared to Pt (111) surface. Surprisingly, the energy barriers for $H_2$ dissociation and $H_2O$ formation in HOR (the reverse reaction of HER) at the unsaturated Rh sites of $Rh_2Sb$ (210) step were calculated as 0.02 and 0.79 eV, respectively, which were smaller than those of Pt (111) surface (0.15 and 0.82 eV). Since the unsaturated surface steps on Pt may have higher activity than the crystalline (111) surface,[41–43] the adsorption structures of $H_2O$ and $H_2$ on Pt (211) surface were compared with that on the $Rh_2Sb$ (210) step. We find that the surface-O (in $H_2O$) (2.28 Å) and surface-H (in $H_2$) (1.72 Å) distances on $Rh_2Sb$ (210) step are also smaller than that on Pt (211) surface (calculated as 2.30 and 3.10 Å, respectively), implying a lowered reaction barrier for $H_2O/H_2$ dissociation and increased HOR/HER activities on the $Rh_2Sb$ (210) surface. Combined with XPS spectra suggest that there is an upshift of the *d*-band center of the surface Rh atoms in $Rh_2Sb$ NBs relative to the Rh NBs (Figure S5, Supporting Information), demonstrating increased adsorption of $H_2O$ and $H_2$ on the $Rh_2Sb$ step and thus higher HOR/HER activities. Finally, to simulate a more realistic alkaline condition in reactions, we have also incorporated a bilayer of water molecules along with $Na^+$ cations on $Rh_2Sb$ (210) surface in DFT calculations, as shown Figure S18, Supporting Information. We found that the HOR reaction energy barrier in the Volmer step ($H_2O$ formation) was further reduced from 0.79 to 0.66 eV. Thus, the inclusion of the alkaline solvent effect affirms our DFT results and lends strong support to the experimental observations.

## 3. Conclusion

In summary, we have successfully fabricated a class of highly branched $Rh_2Sb$ NBs with atomically isolated Rh sites as high-performance electrocatalysts toward alkaline HOR/HER. $Rh_2Sb$ NBs/C exhibited superior HER performance to Rh NBs/C and commercial Pt/C. Strikingly, $Rh_2Sb$ NBs/C also displayed excellent HOR performance and promising resistance to CO poisoning, of which the HOR specific activity and mass activity were ≈9.9 and ≈10.1 times to those of Rh NBs/C, and ≈4.2 and ≈3.7 times to those of Pt/C, respectively. DFT calculations revealed that the unsaturated Rh sites on $Rh_2Sb$ NBs step were uniquely responsible for the enhanced alkaline HER and HOR activities. This work provides a new strategy for designing highly active and stable HOR/HER electrocatalysts by combining atomically isolated surface sites and unique alloy structure, but also promotes the fundamental researches on electrocatalyst design for anion exchange membrane fuel cells, water electrolysis, and beyond.

## Supporting Information

Supporting Information is available from the Wiley Online Library or from the author.

## Acknowledgements

Y.Z., G.L., and Z.Z. contributed equally to this work. This work was financially supported by the Ministry of Science and Technology of China (2017YFA0208200, 2016YFA0204100), the National Natural Science Foundation of China (22025108), and start-up supports from University of California, Irvine (H.L.X.) and Xiamen University (X.H.). The work at California State University Northridge was supported by the NSF-PREM program (DMR-1828019).

## Conflict of Interest

The authors declare no conflict of interest.

## Data Availability Statement

Research data are not shared.

## Keywords

hydrogen evolution reaction, hydrogen oxidation reaction, isolated site, nanobranch, $Rh_2Sb$

Received: July 1, 2021
Revised: July 20, 2021
Published online: September 12, 2021

[1] J. A. Turner, *Science* **2004**, *305*, 972.
[2] M. S. Dresselhaus, I. L. Thomas, *Nature* **2001**, *414*, 332.
[3] J. Mahmood, F. Li, S.-M. Jung, M. S. Okyay, I. Ahmad, S.-J. Kim, N. Park, H. Y. Jeong, J.-B. Baek, *Nat. Nanotechnol.* **2017**, *12*, 441.
[4] P. Xiao, W. Chen, X. Wang, *Adv. Energy Mater.* **2015**, *5*, 1500985.
[5] Y. Xue, L. Shi, X. Liu, J. Fang, X. Wang, B. P. Setzler, W. Zhu, Y. Yan, Z. Zhuang, *Nat. Commun.* **2020**, *11*, 5651.
[6] J. Yang, W. Li, D. Wang, Y. Li, *Adv. Mater.* **2020**, *32*, 2003300.
[7] Y. Shi, J. Wang, C. Wang, T. T. Zhai, W. J. Bao, J. J. Xu, X. H. Xia, H. Y. Chen, *J. Am. Chem. Soc.* **2015**, *137*, 7365.
[8] Y. Zheng, Y. Jiao, Y. Zhu, L. H. Li, Y. Han, Y. Chen, M. Jaroniec, S. Z. Qiao, *J. Am. Chem. Soc.* **2016**, *138*, 16174.
[9] E. Liu, J. Li, L. Jiao, H. T. T. Doan, Z. Liu, Z. Zhao, Y. Huang, K. M. Abraham, S. Mukerjee, Q. Jia, *J. Am. Chem. Soc.* **2019**, *141*, 3232.
[10] J. Yang, W.-H. Li, S. Tan, K. Xu, Y. Wang, D. Wang, Y. Li, *Angew. Chem., Int. Ed.* **2021**, *60*, 19085.
[11] D. R. Dekel, *J. Power Sources* **2018**, *375*, 158.
[12] F. Song, W. Li, J. Yang, G. Han, P. Liao, Y. Sun, *Nat. Commun.* **2018**, *9*, 4531.
[13] J. Zheng, W. Sheng, Z. Zhuang, B. Xu, Y. Yan, *Sci. Adv.* **2016**, *2*, e1501602.

 

[14] Q. Li, H. Peng, Y. Wang, L. Xiao, J. Lu, L. Zhuang, *Angew. Chem., Int. Ed.* **2019**, *58*, 1442.
[15] S. Lu, Z. Zhuang, *Sci. China Mater.* **2016**, *59*, 217.
[16] J. R. Varcoe, P. Atanassov, D. R. Dekel, A. M. Herring, M. A. Hickner, P. A. Kohl, A. R. Kucernak, W. E. Mustain, K. Nijmeijer, K. Scott, T. Xu, L. Zhuang, *Energy Environ. Sci.* **2014**, *7*, 3135.
[17] W. Sheng, H. A. Gasteiger, Y. J. Shao-Horn, *Electrochem. Soc.* **2010**, *157*, B1529.
[18] S. Lu, Z. Zhuang, *J. Am. Chem. Soc.* **2017**, *139*, 5156.
[19] J. K. Nørskov, T. Bligaard, Á. Logadóttir, J. R. Kitchin, J. G. Chen, S. Pandelov, U. Stimming, *J. Electrochem. Soc.* **2005**, *152*, J23.
[20] Y. Jin, F. Chen, J. Wang, L. Guo, T. Jin, H. Liu, *J. Power Sources* **2019**, *435*, 226798.
[21] L. Su, Y. Zhao, F. Yang, T. Wu, G. Cheng, W. Luo, *J. Mater. Chem. A* **2020**, *8*, 11923.
[22] C. Zhang, H. Liu, Y. Liu, X. Liu, Y. Mi, R. Guo, J. Sun, H. Bao, J. He, Y. Qiu, J. Ren, X. Yang, J. Luo, G. Hu, *Small Methods* **2020**, *4*, 2000208.
[23] C. Z. Wan, X. F. Duan, Y. Huang, *Adv. Energy Mater.* **2020**, *10*, 1903815.
[24] J. Li, S. G. Chen, N. Yang, M. M. Deng, S. Ibraheem, J. H. Deng, J. Li, L. Li, Z. Wei, *Angew. Chem., Int. Ed.* **2019**, *58*, 7035.
[25] B. Qiao, A. Wang, X. Yang, L. F. Allard, Z. Jiang, Y. Cui, J. Liu, J. Li, T. Zhang, *Nat. Chem.* **2011**, *3*, 634.
[26] Y. Zhang, L. Guo, L. Tao, Y. Lu, S. Wang, *Small Methods* **2019**, *3*, 1800406.
[27] C. Zhu, S. Fu, Q. Shi, D. Du, Y. Lin, *Angew. Chem., Int. Ed.* **2017**, *56*, 13944.
[28] T. J. Zhang, A. G. Walsh, J. H. Yu, P. Zhang, *Chem. Soc. Rev.* **2021**, *50*, 569.
[29] N. Zhang, L. G. Li, J. Wang, Z. W. Hu, Q. Shao, X. H. Xiao, X. Q. Huang, *Angew. Chem., Int. Ed.* **2020**, *59*, 8066.
[30] J. Zhang, J. Ye, Q. Fan, Y. Jiang, Y. Zhu, H. Li, Z. Cao, Q. Kuang, J. Cheng, J. Zheng, Z. Xie, *J. Am. Chem. Soc.* **2018**, *140*, 11232.
[31] R. T. Hannagan, G. Giannakakis, M. Flytzani-Stephanopoulos, E. C. H. Sykes, *Chem. Rev.* **2020**, *120*, 12044.
[32] C. Liu, J. Qian, Y. Ye, H. Zhou, C. J. Sun, C. Sheehan, Z. Zhang, G. Wan, Y. S. Liu, J. Guo, S. Li, H. Shin, S. Hwang, T. B. Gunnoe, W. A. GoddardIII, S. Zhang, *Nat. Catal.* **2021**, *4*, 36.
[33] J. Liao, W. Ding, S. Tao, Y. Nie, W. Li, G. Wu, S. Chen, L. Li, Z. Wei, *Chin. J. Catal.* **2016**, *37*, 1142.
[34] Q. H. Wu, S. G. Sun, X. Y. Xiao, Y. Y. Yang, Z. Y. Zhou, *Electrochim. Acta* **2000**, *45*, 3683.
[35] Z. Zhuang, S. A. Giles, J. Zheng, G. R. Jenness, S. Caratzoulas, D. G. Vlachos, Y. Yan, *Nat. Commun.* **2016**, *7*, 10141.
[36] Y. F. Tang, H. M. Zhang, H. X. Zhong, Z. Xu, *Int. J. Hydrogen Energy* **2012**, *37*, 2129.
[37] Y. Zhou, Z. Xie, J. Jiang, J. Wang, X. Song, Q. He, W. Ding, Z. Wei, *Nat. Catal.* **2020**, *3*, 454.
[38] Z. Feng, L. Li, X. Zheng, J. Li, N. Yang, W. Ding, Z. Wei, *J. Phys. Chem. C* **2019**, *123*, 23931.
[39] P. S. Lamoureux, A. R. Singh, K. Chan, *ACS Catal.* **2019**, *9*, 6194.
[40] L. Zhao, H. Liu, Y. Liu, X. Han, J. Xu, W. Xing, W. Guo, *ACS Appl. Mater. Interfaces* **2020**, *12*, 40248.
[41] C. L. Bentley, M. Kang, F. M. Maddar, F. Li, M. Walker, J. Zhang, P. R. Unwin, *Chem. Sci.* **2017**, *8*, 6583.
[42] H. Li, C. Tsai, A. L. Koh, L. Cai, A. W. Contryman, A. H. Fragapane, J. Zhao, H. S. Han, H. C. Manoharan, F. Abild-Pedersen, *Nat. Mater.* **2016**, *15*, 48.
[43] G. Gao, Q. Sun, A. Du, *J. Phys. Chem. C* **2016**, *120*, 16761.